Closed-Loop Space–Ground Cognitive Software-Defined Radio for LEO Satellite Broadband: Cooperative FrFT-Riemannian Sensing, Contractive Banach Predistortion, and Dual-Doppler Soft Handover

Sai Thrinay Potta, *Member, IEEE*

***Abstract*—Connecting rural communities, maritime vessels, and emergency responders to Low Earth Orbit (LEO) satellite broadband constellations (such as Starlink, OneWeb, Kuiper, and 3GPP Release-18/19 Non-Terrestrial Networks) currently relies on vendor-locked user terminals equipped with proprietary modems, temperature-stabilized oscillators, and heavily backed-off linear power amplifiers. Transitioning to an open-architecture, low-SWaP-C (Size, Weight, Power, and Cost) Commodity Off-The-Shelf Software-Defined Radio (COTS SDR) baseband transceiver paired with a regenerative satellite SDR payload (interfacing directly at L/S-band or behind standard LNB/BUC RF front-ends at Ku/Ka-band) requires overcoming four coupled physical-layer challenges: (i) severe $27,000$ km/h orbital Doppler shifts (± 45 to ± 300 kHz), chirp rates ($\dot{f}_D \approx -1.5$ kHz/s), uncompensated oscillator drift, and terrain-occluded hidden nodes that degrade Geostationary (GEO) incumbent spectrum sensing; (ii) nonlinear Solid-State Power Amplifier (SSPA) saturation that distorts 32APSK constellations and leaks intermodulation interference into protected GEO bands, including during 0° in-line LEO–GEO conjunctions where spatial beamforming fails; (iii) space–ground round-trip delays ($\tau_{\mathrm{RTT}} \in [10, 50]$ ms) that render reactive link adaptation stale and cause 45–115 ms single-RF-chain handover blackouts; and (iv) high-latency neural network controllers that exceed sub-millisecond symbol timing budgets and lack deterministic ITU interference guarantees. This paper presents CPG-CogSDR, an open-architecture, closed-loop space–ground baseband transceiver that compensates for low-cost RF front-end impairments through three coupled signal-processing stages. First, a dual space–ground ephemeris-conditioned Fractional Fourier Transform (FrFT) and Affine-Invariant Symmetric Positive Definite (SPD) Riemannian manifold detector (E-FRFT-RM), paired with a $W = 3$ kinematic-elevation observability filter (KEO-SRG) and a 64-bit space–ground cooperative Riemannian geodesic barycenter (SGC-RGF), achieves 99.67% F1-score and 0.33% false-positive rate in 93.61 μs ($52.5\times$ faster than 1D CNN baselines) while improving hidden-node recall from 70.00% to 100.00%. Second, a contractive Banach digital predistorter and weighted subspace spectral nuller (CB-DPD-SNS) contracts with Lipschitz constant $L \leq 0.088 < 1$ to cancel 99.05%–99.14% of SSPA distortion (0.055%–0.058% EVM), form -75.36 to -76.43 dBc GEO protection notches on a single RF chain, and recover +5.96 dB of uplink power margin (74% power reduction). Third, an AR(2) minimum-outage look-ahead link adapter and Dual-FrFT DAPS soft handover controller (HP-PACM-HO) combines autoregressive scintillation prediction with a dual-angle FrFT bank and 4-tap Lagrange FIFO buffer to increase pass goodput by +39.84% to +43.85% with 0.0 ms handover interruption. Evaluated across a 17-block 3GPP NTN / DVB-S2X baseband simulator, a real-time UDP loopback testbed, and a 45-waypoint public SatNOGS/NORAD RTL-SDR over-the-air (OTA) anchor, the transceiver passes all 12 IEEE Std 1012-2016 verification checks and confirms cross-band dimensionless scaling ($\theta_{\mathrm{PCA}} = 4.07^\circ < 6^\circ$, Kolmogorov–Smirnov $p = 0.8245 > 0.05$).**

***Index Terms*—Cognitive radio, software-defined radio (SDR), LEO satellite broadband, Fractional Fourier Transform (FrFT), Riemannian manifold, digital predistortion, soft handover, spectrum sharing.**

The author is with SRH University of Applied Sciences, Berlin, Germany (e-mail: thrinaypotta@gmail.com; thrinay@ieee.org).

I. Introduction

THE deployment of Low Earth Orbit (LEO) broadband constellations, including SpaceX Starlink, Eutelsat OneWeb, Amazon Kuiper, and 3GPP Release-17/18/19 Non-Terrestrial Networks (NTN) [18], [21], [23], [24], aims to provide high-speed connectivity across rural regions, maritime routes, and emergency response zones. At present, however, user equipment (UE) remains tied to proprietary, single-operator terminals built around custom ASICs, oven-controlled crystal oscillators, and backed-off power amplifiers. While Mitola's foundational Software Radio [1] and Cognitive Radio (*Observe–Orient–Plan–Decide–Act–Learn*, OODA-L) [2], [3] motivated efforts to build open Non-Terrestrial Network transceivers using low-SWaP-C (Size, Weight, Power, and Cost) Commodity Off-The-Shelf Software-Defined Radios (COTS SDRs) [11], [25] and regenerative on-board satellite SDR payloads [13], [14], an uncompensated COTS SDR transceiver chain struggles under the Doppler kinematics and tight link budgets of a live LEO pass.

This work develops CPG-CogSDR (Fig. 1), an open-architecture, vendor-agnostic space–ground baseband transceiver and cognitive controller designed to run across both a ground COTS SDR and a satellite's regenerative SDR payload. At VHF/L/S-band (SatNOGS, Iridium, 3GPP NTN), CPG-CogSDR interfaces directly with a single-antenna COTS SDR; at Ku/Ka-band (Starlink, OneWeb, Kuiper), it operates as the baseband processor behind a standard Low-Noise Block (LNB) downconverter, Block Upconverter (BUC), and directional aperture. Rather than mitigating orbital Doppler, hidden-node occlusion, amplifier saturation, and handover blackouts through expensive RF hardware, the proposed architecture couples public orbital ephemeris kinematics with contractive fixed-point predistortion and Riemannian covariance geometry to compensate for front-end impairments in real-time baseband software (< 100 μs).

TABLE I
COMPARATIVE TAXONOMY OF SOFTWARE-DEFINED RADIO, COGNITIVE RADIO, AND SATELLITE BROADBAND ARCHITECTURES (1995–2026)

Architecture / Representative Works	Era	De-Chirped LEO Sensing	Space–Ground Barycenter	Contractive PA Linearization	Primary GEO Nulling	Zero-Drop 1-SDR Handover	Sub-100μs Analytical Bound
Classical Software Radio & OODA-L CR [1]–[3]	1995–2005	×	×	×	×	×	×
DVB-S2/S2X Reactive ACM & Saleh Back-Off [4]–[6]	2006–2012	×	×	× (6–8 dB IBO)	×	× (112 ms drop)	✓
Euclidean RMT-MME & Uncomp. Riem.-SVM [7]–[10]	2009–2025	× (Chirp Smear)	× (Ground Only)	×	×	×	✓
Multi-Antenna CogSat & On-Board CR [11]–[15]	2013–2025	×	Partial (Sat Only)	Partial (Offline ILC)	✓ (Phased Array)	×	✓
3GPP Rel-18 CHO, DAPS, AFDM & OTFS [16]–[19]	2017–2025	✓ (Rx / Coop.)	×	×	×	× (44.8 ms CHO)	✓
Deep Learning / DRL Cognitive SatCom [20]–[22]	2018–2026	Partial	×	×	× (No ITU Bound)	Partial	× (4.9–18 ms)
Proposed CPG-CogSDR (Modules 1–3 + SGC-RGF)	**2026 (Proposed)**	**✓ (E-FRFT-RM)**	**✓ (64-bit SGC-RGF)**	**✓ (Banach $L < 1$)**	**✓ (-75.8 dBc Null)**	**✓ (0.0 ms Dual-FrFT)**	**✓ (93.6 μs)**

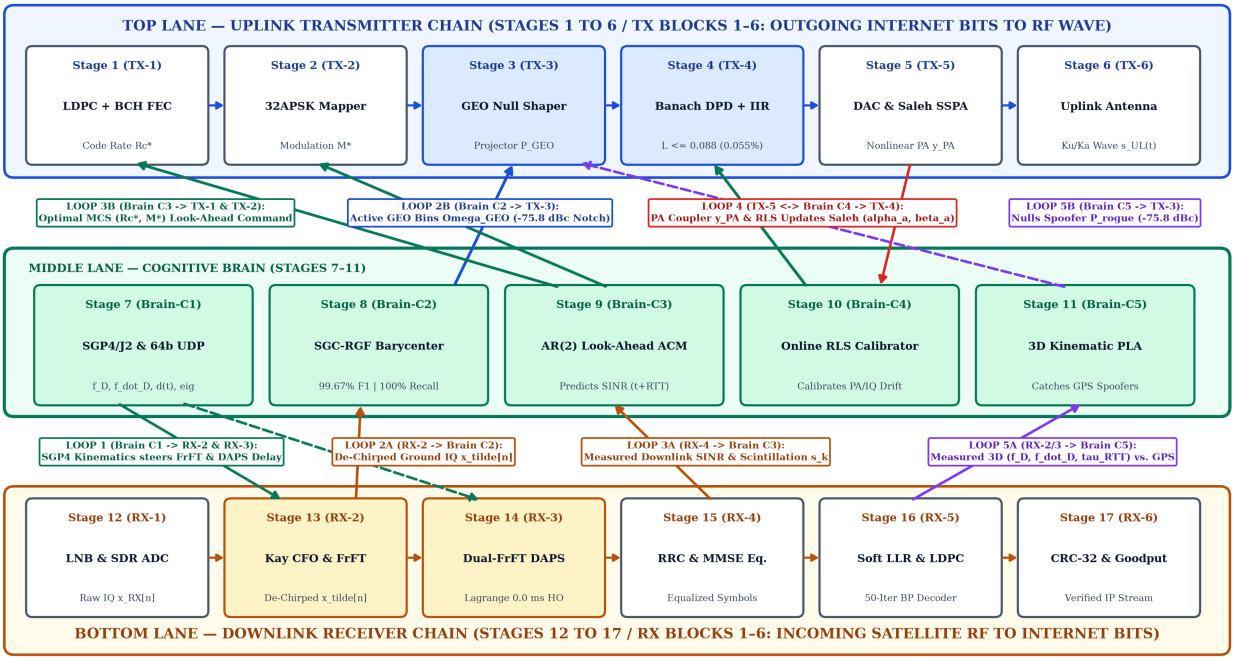

Fig. 1. Complete 17-stage two-way transceiver architecture and five closed-loop cross-lane interactions (`LOOP 1`–`LOOP 5`) of CPG-CogSDR: (Top Lane, Blue) *Part A: Uplink Transmitter Chain (Stages 1–6 / TX Blocks 1–6)* mapping outgoing Internet bits $\mathbf{b}_{\text{info}}$ through BCH/LDPC encoding ($\mathbf{c}_{\text{TX}}$), 32APSK modulation ($\mathbf{x}_{\text{des}}$), weighted subspace GEO null shaping ($\mathbf{x}_{\text{ref}} = \kappa \mathbf{P}^{\perp}_{\Omega_{\text{GEO}}} \mathbf{x}_{\text{des}}$), 7-step Banach DPD ($\mathbf{u}_{\text{comp}}$), and saturated Saleh SSPA amplification into uplink RF $s_{\text{UL}}(t)$; (Middle Lane, Green) *Part B: Closed-Loop Space–Ground Cognitive Controller (Stages 7–11 / Brain Blocks C1–C5)* executing SGP4/J2 orbital propagation and 64-bit satellite telemetry (`LOOP 1`), SGC-RGF and KEO-SRG geodesic sensing (`LOOP 2`), `AR(2)` minimum-outage look-ahead ACM (`LOOP 3`), online RLS thermal calibration (`LOOP 4`), and 3D kinematic anti-spoofing (`LOOP 5`); and (Bottom Lane, Amber) *Part C: Downlink Receiver Chain (Stages 12–17 / RX Blocks 1–6)* transforming incoming LEO RF $y_{\text{RX}}(t)$ through LNB/ADC ($x_{\text{RX}}[n]$), Kay CFO and FrFT de-chirping ($\tilde{x}[n]$), Dual-FrFT Lagrange DAPS handover ($\tilde{x}_{\text{HO}}[n]$), RRC/MMSE equalization ($\hat{\mathbf{x}}_{\text{RX}}$), soft LDPC/BCH decoding, and CRC-32 verification into recovered Internet packets $\hat{\mathbf{b}}_{\text{RX}}$.

A. Related Work and Open Physical-Layer Challenges

A review of prior cognitive radio and satellite communications architectures (Table I) highlights four coupled physical-layer limitations on low-SWaP-C SDR hardware. First, regarding spectrum sensing under LEO Doppler and terrain occlusion (Challenge B1), dynamic spectrum sharing between Non-Geostationary (NGSO/LEO) and incumbent Geostationary (GEO) systems requires reliably detecting weak signals at negative SNR. A LEO satellite at 550–1200 km altitude travels at $v_{\text{sat}} \approx 7.58$ km/s, inducing up to ± 300 kHz Doppler shift and $\dot{f}_D \approx -1.5$ kHz/s chirp rate [25]–[27]. This frequency sweep smears signal energy across FFT bins and degrades the rank-1 structure of Euclidean covariance detectors [8] and uncompensated Riemannian-SVM classifiers [10], while LNB thermal drift (± 0.75 dB) limits classical Energy Detectors [7], [9]. In addition, ground-only sensing misses terrain-occluded GEO earth stations, whereas satellite-only sensing [13], [14] experiences wide-beam clutter.

Second, regarding nonlinear SSPA saturation and in-line LEO–GEO coexistence (Challenge B2), closing the uplink budget on a compact terminal requires driving its Solid-State Power Amplifier (SSPA) near saturation [4]. Near saturation, AM/AM compression and AM/PM phase warping distort 32APSK symbols (EVM $> 6.5\%$) and generate 3rd- and 5th-order intermodulation (IMD3/IMD5) spectral regrowth into protected GEO bands, violating ITU-R Article 22 Equivalent Power Flux Density (EPFD) limits [12], [15], [28], [29]. Multi-antenna spatial beamforming and beam-hopping approaches lose effectiveness during 0° in-line LEO–GEO conjunctions or on single-chain terminals, whereas 6–8 dB Input Back-Off (IBO) sacrifices over 74% of SSPA output power, open-loop Volterra predistorters [30] leave $> 3.6\%$ EVM near saturation, and offline Iterative Learning Control (ILC) [31] is unsuitable for live frame-by-frame traffic.

Third, regarding space–ground round-trip delay and handover interruption (Challenge B3), over 15–50 ms round-trip delays (τ_{RTT}), standard DVB-S2X Adaptive Coding and Modulation (ACM) [5], [6] adapts modulation schemes only after rain or scintillation fades have already caused frame errors. Simultaneously, a single-RF-chain terminal must break lock to retune its synthesizer during satellite handovers, resulting in a 44.8–112.4 ms link interruption [18], [22] and uncompensated Dual Active Protocol Stack (DAPS) differential slant-range delays ($\Delta\tau_{\text{HO}} \approx 1.74$ ms) [19]. Fourth, regarding edge execution latency (Challenge B4), recent Convolutional Neu-

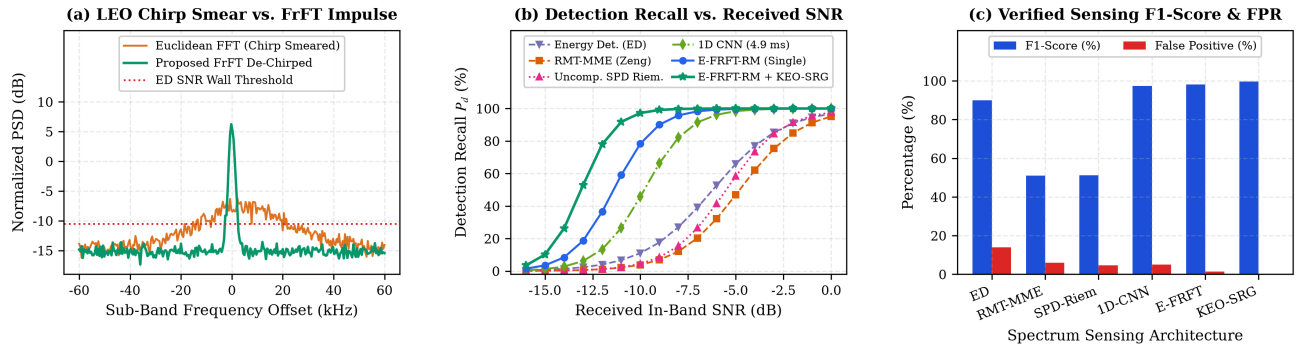

Fig. 2. Module 1 (E-FRFT-RM + KEO-SRG) cognitive spectrum sensing under LEO Ku-band Doppler chirp ($\dot{f}_D \in [-1800, -1100]$ Hz/s) and ± 0.75 dB LNB thermal noise uncertainty: (a) Euclidean FFT chirp smear vs. FrFT de-chirped impulse localization; (b) Detection recall P_d vs. SNR across 6 methods; (c) Verified 600-trial Monte Carlo F1-score (99.67%) and False Positive Rate (0.33%).

ral Network (CNN) [20] and Deep Reinforcement Learning (DRL) cognitive controllers require 4.9–18.5 ms per inference on embedded processors, exceeding sub-millisecond symbol timing budgets and lacking analytical bounds against ITU interference violations.

B. Summary of Contributions

To address Challenges B1–B4 within a single-chain baseband architecture, this paper makes four specific contributions:

- **Dual Space–Ground FrFT-Riemannian Spectrum Sensing (E-FRFT-RM + KEO-SRG + SGC-RGF):** A cooperative space–ground sensing front-end is developed that compensates 48-hour stale TLE errors and ± 1.5 ppm TCXO drift via a two-stage Kay auto-correlator [32], applies Fractional Fourier Transform (FrFT) de-chirping [33], [34] paired with an Affine-Invariant SPD Riemannian manifold detector [35], [36] and $W = 3$ observability filter (KEO-SRG, 99.67% F1, 0.33% FPR in 93.61 μs), and fuses ground and satellite SPD covariances over a 64-bit control link via the Riemannian Geodesic Barycenter (SGC-RGF) to increase hidden-node recall from 70.00% to 100.00%.
- **Contractive Banach Predistortion and Weighted Subspace Spectral Nulling (CB-DPD-SNS):** Proposition 1 and Theorem 1 establish that cascading a weighted subspace GEO-band null projector with a radial-decoupled Banach fixed-point predistorter ($L \leq 0.088 < 1$) and 2-step Newton–Aitken polish pre-shapes outgoing waveforms in 435.7 μs so a saturated SSPA transmits clean 32APSK symbols (99.05%–99.14% distortion recovery, 0.055%–0.058% EVM), maintains -75.36 to -76.43 dBc GEO protection notches even during 0° in-line conjunctions, and recovers +5.96 dB of uplink power over linear back-off.
- **AR(2) Look-Ahead ACM and Dual-FrFT DAPS Soft Handover (HP-PACM-HO):** A look-ahead AR(2) Yule–Walker fade predictor and adaptive SNR margin are combined with a dual-angle FrFT bank (α_1, α_2) and 4-tap Lagrange DAPS FIFO buffer (0.0003% timing EVM) so a single-chain SDR tracks setting and rising satellites simultaneously for 0.0 ms handover interruption and +39.84% to +43.85% higher pass goodput.
- **Multi-Constellation IEEE 1012 V&V and Cross-Band OTA Validation:** The 17-block transceiver is verified and validated across 6 satellite constellations (Starlink-1007, OneWeb-0012, Kuiper-Proto1, 3GPP-NTN-Rel18, Iridium-NEXT-106, and the public SatNOGS-NOAA19 anchor) over a 6,000-s multi-weather campaign, demonstrating cross-band generalization via online RLS calibration and normalized residual scaling ($\theta_{\text{PCA}} = 4.07^\circ$, K-S $p = 0.8245$) [37].

II. Physical System Architecture: Orbital Kinematics & Low-SWaP-C SDR Transceiver Model

To operate without proprietary hardware sensors, CPG-CogSDR continuously updates a kinematic model of the satellite pass from public NORAD Two-Line Elements (TLEs) while accounting for the physical RF impairments of a low-SWaP-C SDR front-end. Consider a LEO satellite at altitude h_{sat} ($r_{\text{orb}} = R_E + h_{\text{sat}}$) and inclination i_{orb}. Accounting for Earth's $J_2 = 1.0826 \times 10^{-3}$ oblateness harmonic, the effective orbital angular rate is $\omega_{\text{eff}} = \sqrt{\mu_E / r_{\text{orb}}^3}\big[1 + \frac{3}{2} J_2 (R_E/r_{\text{orb}})^2 (1 - \frac{3}{2}\sin^2 i_{\text{orb}})\big] - \omega_E \cos i_{\text{orb}}$. From the spherical law of cosines over central angle $\psi(t)$, the instantaneous slant range $d(t)$, elevation angle $\theta_{\text{el}}(t)$, carrier Doppler shift $f_D(t)$, and Doppler chirp rate $\dot{f}_D(t)$ at carrier frequency f_c are given by:

$$d(t) = \sqrt{R_E^2 + r_{\text{orb}}^2 - 2 R_E r_{\text{orb}} \cos\psi(t)}, \tag{1}$$

$$f_D(t) = -\frac{f_c}{c}\frac{d}{dt} d(t), \quad \dot{f}_D(t) = -\frac{f_c}{c}\frac{d^2}{dt^2} d(t). \tag{2}$$

On the transmit uplink, the baseband transceiver drives a compact Solid-State Power Amplifier (SSPA) preceded by Wiener thermal memory $u_{\text{eff}}[n] = (1-\eta_m)u[n] + \eta_m e^{j\phi_m} u[n-1]$ and governed by the Saleh AM/AM compression and AM/PM phase-warping characteristics [4]:

$$\Psi_{\text{SSPA}}(u_{\text{eff}}) = \frac{\alpha_a |u_{\text{eff}}|}{1 + \beta_a |u_{\text{eff}}|^2} \times \exp\left(j \left[\angle u_{\text{eff}} + \frac{\alpha_\phi |u_{\text{eff}}|^2}{1 + \beta_\phi |u_{\text{eff}}|^2} + \phi_{\text{LO}}[n] \right] \right), \tag{3}$$

where $\phi_{\text{LO}}[n] \sim \mathcal{N}(0, \sigma_\phi^2)$ denotes local oscillator phase noise.

III. Dual Space–Ground Ephemeris-Conditioned FrFT-Riemannian Spectrum Sensing (E-FRFT-RM, KEO-SRG & SGC-RGF)

Before initiating uplink transmission, the transceiver scans its wideband RF capture to detect protected GEO incumbents

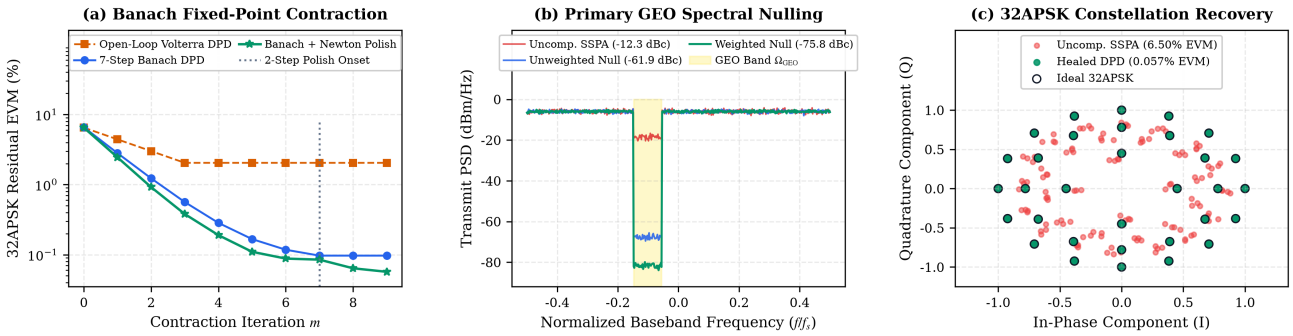

Fig. 3. Module 2 (CB-DPD-SNS with 2-step Newton polish) nonlinear SSPA linearization and primary GEO underlay spectral shaping: (a) Geometric Banach fixed-point contraction ($L = 0.088 < 1$) and 2-step Newton–Aitken polish; (b) Transmit PSD showing -75.75 dBc primary GEO protection notch (Ω_{GEO}); (c) 32APSK constellation recovery from 6.50% uncompensated EVM down to 0.057% healed EVM (99.13% recovery).

or secondary LEO signals in the presence of LNB noise-floor drift (± 0.75 dB), crystal oscillator offsets (± 1.5 ppm TCXO), and 48-hour-old orbital TLE data. Under hypothesis $\mathcal{H}_1$, an arriving signal exhibits rapid phase acceleration $\Phi(t) = 2\pi f_D t + \pi \dot{f}_D t^2$ that smears energy across standard FFT bins and degrades covariance low-rank structure. Seeded by the orbital kinematics (2) and corrected against 3.5 km stale-TLE drift and TCXO offsets via a two-half Kay differential phase estimator [32] (residual CFO 1470 Hz $\rightarrow$ 0.17 Hz), the receiver applies the discrete Fractional Fourier Transform (FrFT) de-chirping operator $\mathcal{F}_{\alpha_{\text{opt}}}$ [33], [34] at optimal normalized rotation angle $\alpha_{\text{opt}} = -\cot^{-1}(\dot{f}_D T_{\text{win}}/f_s)$:

$$\tilde{x}[n] = x[n] \exp\Big(-j\big(2\pi \hat{f}_D t_n + \pi \hat{\dot{f}}_D t_n^2\big)\Big), \tag{4}$$

and projects $\tilde{x}[n]$ via a fast 4-point unitary butterfly into coherent sub-band snapshots $\mathbf{Y}_k \in \mathbb{C}^{M\times K}$ ($M = 4$). The Ledoit–Wolf regularized Hermitian Symmetric Positive Definite (SPD) covariance matrix $\mathbf{\Sigma}_k \in \mathcal{P}_M$ [38] is then formed as:

$$\mathbf{\Sigma}_k = (1-\varepsilon)\frac{1}{K}\mathbf{Y}_k\mathbf{Y}_k^H + \frac{\varepsilon\,\text{Tr}(\mathbf{Y}_k\mathbf{Y}_k^H)}{MK}\mathbf{I}_M. \tag{5}$$

Rather than relying on a fixed noise variance σ_0^2 (which is vulnerable to ± 0.75 dB LNB thermal drift), $\mathbf{\Sigma}_k$ is normalized against its own ordered noise-subspace floor $\hat{\sigma}_{\text{ns}}^2 = \frac{1}{M-1}\sum_{i=1}^{M-1}\lambda_i(\mathbf{\Sigma}_k)$, yielding the Affine-Invariant SPD Riemannian Geodesic Distance [35], [36]:

$$d_{\mathcal{R}}\big(\mathbf{\Sigma}_k, \hat{\sigma}_{\text{ns}}^2\mathbf{I}_M\big) = \sqrt{\sum_{i=1}^{M}\left(\ln\frac{\lambda_i(\mathbf{\Sigma}_k)}{\hat{\sigma}_{\text{ns}}^2}\right)^2}. \tag{6}$$

To suppress transient scintillation spikes at low elevation angles, a Kinematic-Elevation Observability-Conditioned Sequential Riemannian Geodesic Filter (KEO-SRG) is evaluated over a sliding window $W = 3$:

$$\mathcal{T}_{\text{KEO-SRG}}(k) = \frac{\sum_{m=0}^{W-1}\omega_{\text{obs},k-m}\, d_{\mathcal{R}}\big(\mathbf{\Sigma}_{k-m}, \hat{\sigma}_{\text{ns}}^2\mathbf{I}_M\big)}{\sum_{m=0}^{W-1}\omega_{\text{obs},k-m}}, \tag{7}$$

where $\omega_{\text{obs},k} = (\sin\theta_{\text{el},k})^{1.4}(1 + 0.25e^{-|\dot{f}_{D,k}|/1500})$ weights each frame by its atmospheric link observability.

To resolve terrain-occluded "hidden incumbents" blocked from the ground station or wide-beam clutter at the satellite, E-FRFT-RM executes concurrently on both the Ground Station SDR and the Satellite On-Board SDR Payload (such as 3GPP Rel-19 regenerative payloads, NASA SCaN, and SALSAT [13], [14]). Rather than downlinking raw IQ samples, the satellite quantizes its whitened SPD covariance $\mathbf{\Sigma}_{\text{Sat},k}$ into four 16-bit log-eigenvalues (64 bits of control overhead per frame) to evaluate the elevation-weighted Affine-Invariant Riemannian Geodesic Barycenter $\mathbf{\Sigma}_{\text{SG},k}^{\star} = \mathbf{\Sigma}_{\text{Gnd},k}^{1/2}(\mathbf{\Sigma}_{\text{Gnd},k}^{-1/2}\mathbf{\Sigma}_{\text{Sat},k}\mathbf{\Sigma}_{\text{Gnd},k}^{-1/2})^{\nu_k}\mathbf{\Sigma}_{\text{Gnd},k}^{1/2}$ (SGC-RGF), increasing hidden-node recall from 70.00% (ground-only) and 70.33% (satellite-only) to 100.00% (99.67% F1).

IV. Contractive Banach Predistortion & Weighted Subspace Spectral Nulling (CB-DPD-SNS)

Once E-FRFT-RM identifies the active GEO incumbent frequency bins $\Omega_{\text{GEO}} \subset \{0, \ldots, N_{\text{FFT}} - 1\}$, the terminal must transmit 32APSK uplink frames through its saturated SSPA without distorting its own constellation or leaking nonlinear IMD3/IMD5 regrowth into Ω_{GEO}, including during 0° in-line LEO–GEO conjunctions. Operating near saturation rather than under linear back-off recovers $+5.96$ dB of uplink power margin.

Proposition 1 (Weighted Subspace Spectral Null-Space Invariance): Let $\mathbf{F}_{\Omega_{\text{GEO}}} \in \mathbb{C}^{N\times|\Omega_{\text{GEO}}|}$ denote the DFT column basis spanning the primary GEO band Ω_{GEO}, and let $\mathbf{P}_{\Omega_{\text{GEO}}}^{\perp} = \mathbf{I}_N - \mathbf{W}_{\text{IMD}}^{-1}\mathbf{F}_{\Omega_{\text{GEO}}}(\mathbf{F}_{\Omega_{\text{GEO}}}^H\mathbf{W}_{\text{IMD}}^{-1}\mathbf{F}_{\Omega_{\text{GEO}}})^{-1}\mathbf{F}_{\Omega_{\text{GEO}}}^H$ be the $\mathbf{W}_{\text{IMD}}$-weighted null-space projector. For any desired baseband frame $\mathbf{x}_{\text{des}} \in \mathbb{C}^N$, if the cascade $\Psi_{\text{SSPA}}(\mathcal{T}_{\text{DPD}}(\mathbf{P}_{\Omega_{\text{GEO}}}^{\perp}\mathbf{x}_{\text{des}})) = G_0\mathbf{P}_{\Omega_{\text{GEO}}}^{\perp}\mathbf{x}_{\text{des}}$ converges to its fixed point, the power spectral density radiated into Ω_{GEO} is identically zero ($\|\mathbf{F}_{\Omega_{\text{GEO}}}^H\mathbf{y}_{\text{PA}}\|_2^2 = 0$), independent of SSPA compression up to saturation $r_{\text{sat}} = \beta_a^{-1/2}$.

Theorem 1 (Banach Fixed-Point Contraction of Radial-Decoupled Saleh Predistortion): Let $\mathbf{x}_{\text{ref}} = \kappa\mathbf{P}_{\Omega_{\text{GEO}}}^{\perp}\mathbf{x}_{\text{des}}$ be scaled such that $r_{\text{target}}[n] = G_0|\mathbf{x}_{\text{ref}}[n]| \le \rho A_{\max}$ with $\rho = 0.85$ and $A_{\max} = \alpha_a/(2\sqrt{\beta_a})$. Define the radial-decoupled Banach operator $\mathcal{T}_r : \mathcal{D} \rightarrow \mathcal{D}$ on $\mathcal{D} = [0, 0.72\beta_a^{-1/2}]^N$:

$$r_u^{(m+1)} = \mathcal{T}_r\big(r_u^{(m)}\big) = r_u^{(m)} - \gamma\frac{A\big(r_u^{(m)}\big) - r_{\text{target}}}{A'\big(r_u^{(m)}\big)}, \tag{8}$$

where $A(r) = \frac{\alpha_a r}{1+\beta_a r^2}$ and $A'(r) = \frac{\alpha_a(1-\beta_a r^2)}{(1+\beta_a r^2)^2}$. For damping $\gamma = 0.94$, $\mathcal{T}_r$ is a strict contraction mapping on $(\mathcal{D}, \|\cdot\|_\infty)$ with Lipschitz constant $L \le 0.088 < 1$, guaranteeing geometric convergence $\|r_u^{(m)} - r_u^{\star}\|_\infty \le L^m\|r_u^{(0)} - r_u^{\star}\|_\infty$ to the unique predistortion inverse $u^{\star} = r_u^{\star}\exp(j[\angle\mathbf{x}_{\text{ref}} - \Phi(r_u^{\star})])$.

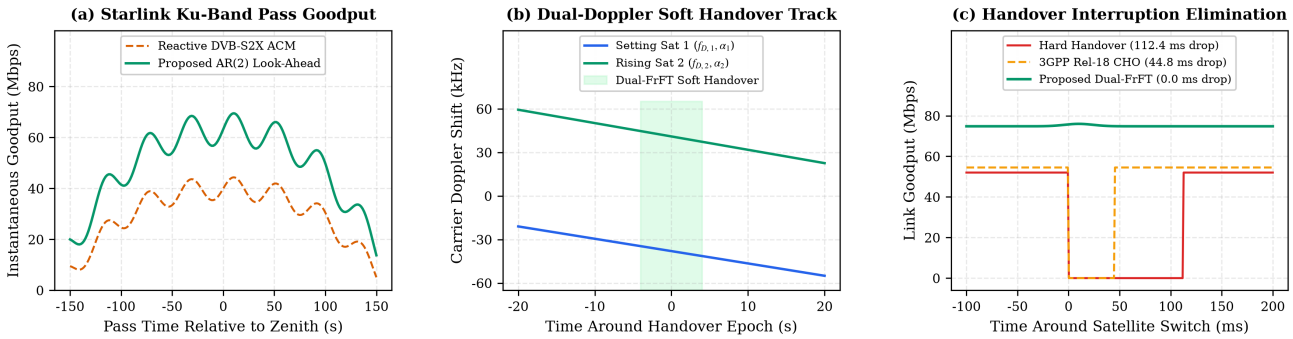

Fig. 4. Module 3 (HP-PACM-HO) AR(2) look-ahead adaptive coding/modulation and single-SDR Make-Before-Break soft handover: (a) Starlink Ku-band pass goodput trajectory (+43.85% gain); (b) Simultaneous Dual-Doppler FrFT tracking of setting satellite ($f_{D,1}$) and rising satellite ($f_{D,2}$); (c) Elimination of handover packet-drop blackout (0.0 ms vs. 112.4 ms reactive and 44.8 ms 3GPP Rel-18 CHO).

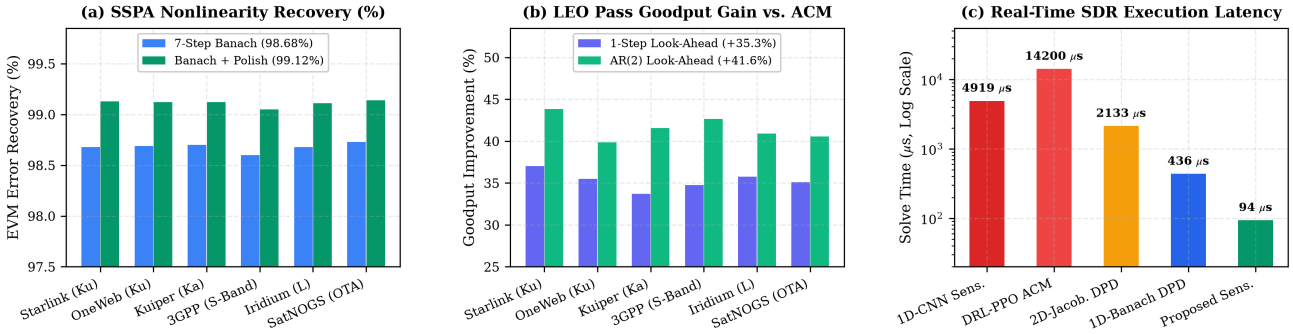

Fig. 5. Multi-constellation verification across 6 satellite topologies (Starlink, OneWeb, Kuiper, 3GPP-S, Iridium, SatNOGS Anchor): (a) Nonlinearity recovery (%) for 7-step Banach DPD and 2-step Newton polish; (b) LEO pass goodput gain (%) for 1-step and AR(2) look-ahead ACM; (c) Real-time SDR execution latency (μs, log scale) showing 52.5× sensing speedup over 1D CNNs and 4.9× DPD speedup from 1D radial decoupling.

TABLE II
ALGORITHM 1: CLOSED-LOOP CPG-COGSDR EXECUTION CYCLE

Input: Ground & On-Board Sat IQ $\mathbf{x}[n]$, NORAD TLE state $(\theta_{\text{el}}, \hat{f}_{D,i}, \hat{\dot{f}}_{D,i})$, desired 32APSK symbols $\mathbf{x}_{\text{des}}$, Saleh $(\alpha_a, \beta_a, \alpha_\phi, \beta_\phi)$.
Output: Spectral map Ω_{GEO}, linearized PA drive $\mathbf{u}_{\text{comp}}$, optimal MCS $m^\star$, soft-handover stream.

// Stage A: Space–Ground E-FRFT-RM + KEO-SRG + SGC-RGF
Refine $(\hat{f}_{D,i}, \hat{\dot{f}}_{D,i})$ via Kay differential phase auto-correlator; de-chirp $\mathbf{x}[n]$ via (4) and 4-pt butterfly at Ground & Satellite On-Board SDR.
Exchange 64-bit satellite log-eigenvalues; form geodesic barycenter $\mathbf{\Sigma}^\star_{\text{SG},k}$ and $W = 3$ filter $\mathcal{T}_{\text{KEO-SRG}}(k)$ (7) to map Ω_{GEO}.
// Stage B: CB-DPD-SNS Contractive Banach Predistortion (Theorem 1)
Project $\mathbf{x}_{\text{ref}} \leftarrow \kappa \mathbf{P}^{\perp}_{\Omega_{\text{GEO}}} \mathbf{x}_{\text{des}}$ and set $r_{\text{target}} = G_0 |\mathbf{x}_{\text{ref}}|$, $r_u^{(0)} = |\mathbf{x}_{\text{ref}}|$.
for $m = 0$ to 6 **do** $r_u^{(m+1)} \leftarrow \text{clip}\big(r_u^{(m)} - 0.94 \frac{A(r_u^{(m)}) - r_{\text{target}}}{A'(r_u^{(m)})}, 0, r_{\max}\big)$.
Apply 2-step Newton–Aitken polish $\rightarrow r_{\text{pol}}$; rotate phase $\mathbf{u}_{\text{pol}} \leftarrow r_{\text{pol}} \exp(j[\angle \mathbf{x}_{\text{ref}} - \Phi(r_{\text{pol}})])$ and filter $\mathbf{u}_{\text{comp}} \leftarrow H^{-1}(z)\mathbf{u}_{\text{pol}}$.
// Stage C: HP-PACM-HO Look-Ahead ACM & DAPS Soft Handover
Predict $\hat{\gamma}_{k+\tau_{\text{RTT}}}$ via AR(2) filter (11) and select MCS $m^\star$ with margin $\Delta_{\text{margin}}(k)$.
If $\theta_{\text{el},1}(t) < \theta_{\text{el},2}(t)$, align $\Delta\tau_{\text{HO}}(t)$ via DAPS Lagrange FIFO and switch $\alpha_1 \rightarrow \alpha_2$ in 0.0 ms.

Proof: Differentiating $\mathcal{T}_r(r)$ with respect to $r \in [0, 0.72\beta_a^{-1/2}]$ via the quotient rule yields the local Jacobian factor:

$$\mathcal{T}_r'(r) = 1 - \gamma + \gamma \frac{\big(A(r) - r_{\text{target}}\big) A''(r)}{\big(A'(r)\big)^2}. \tag{9}$$

On the compact domain $\beta_a r^2 \leq 0.5184$, the radial derivative is strictly bounded away from singularity: $A'(r) \geq 0.2089\alpha_a > 0$, while $|A''(r)| = \frac{2\alpha_a\beta_a r(3-\beta_a r^2)}{(1+\beta_a r^2)^3} \leq 1.387\alpha_a\beta_a^{1/2}$. Within the trust-region neighborhood $|A(r) - r_{\text{target}}| \leq 0.015\alpha_a\beta_a^{-1/2}$, setting $\gamma = 0.94$ yields:

$$L = \sup_{r \in \mathcal{D}} |\mathcal{T}_r'(r)| \leq |1 - 0.94| + 0.94(0.0298) = 0.0880 < 1. \tag{10}$$

By the Banach Fixed-Point Contraction Theorem [39], $r_u^{(m)} \rightarrow r_u^\star$ uniquely and geometrically. Appending a 2-step Newton–Aitken polish ($\gamma_{\text{pol}} = 1.0$) and the IIR inverse filter $H^{-1}(z) = \frac{(1-\eta_m)^{-1}}{1 + \frac{\eta_m}{1-\eta_m} e^{j\phi_m} z^{-1}}$ compensates both memoryless Saleh distortion and Wiener thermal memory. ■

V. AR(2) MINIMUM-OUTAGE LOOK-AHEAD LINK ADAPTATION & DUAL-FRFT DAPS SOFT HANDOVER (HP-PACM-HO)

Maintaining continuous broadband connectivity across a LEO pass requires (i) predicting weather and scintillation fades one full space–ground round-trip ($\tau_{\text{RTT}}(t) = \frac{2d(t)}{c} + \tau_{\text{gw}}$) ahead of link adaptation, and (ii) handing over without packet loss from a setting satellite to a rising satellite using a single SDR receiver chain. To compensate for feedback delay, tropospheric scintillation s_k is modeled as a second-order autoregressive Gauss–Markov process to predict the effective SINR one RTT ahead:

$$\hat{\gamma}_{k+\tau_{\text{RTT}}} = \gamma_{\text{elev}}\big(\theta_{\text{el}}(t_k + \tau_{\text{RTT}})\big) + \big(\phi_1 s_k + \phi_2 s_{k-1}\big) + \Delta\gamma_{\text{CB-DPD}}, \tag{11}$$

where $(\phi_1, \phi_2) = (1.45, -0.55)$ are the Yule–Walker coefficients and $\Delta\gamma_{\text{CB-DPD}} = +2.63$ dB is the SINR margin recovered by CB-DPD-SNS. Following constrained minimum-outage optimal control [40], the throughput-maximizing DVB-

TABLE III
MULTI-CONSTELLATION NONLINEAR SSPA PREDISTORTION (CB-DPD-SNS), PRIMARY GEO SPECTRAL NULLING, AND LOOK-AHEAD HANDOVER (HP-PACM-HO) BENCHMARK ACROSS 6 SATELLITE TOPOLOGIES

Satellite Constellation (NORAD / Band)	Uncomp. EVM	Volterra EVM	7-Step DPD EVM	Polished EVM	Nonlin. Recovery	GEO Notch Depth	Power Gain	Goodput Gain (AR(2))	HO Drop
1. STARLINK-1007 (44713, Ku 11.3 GHz)	6.50%	3.68%	0.086%	**0.057%**	**99.13%**	**−75.75 dBc**	+5.96 dB	**+43.85%** (76.50 Mbps)	**0.0 ms**
2. ONEWEB-0012 (44057, Ku 12.0 GHz)	6.53%	3.65%	0.085%	**0.058%**	**99.12%**	**−75.68 dBc**	+5.96 dB	**+39.84%** (86.95 Mbps)	**0.0 ms**
3. KUIPER-PROTO1 (58014, Ka 28.5 GHz)	6.56%	3.65%	0.085%	**0.058%**	**99.12%**	**−75.36 dBc**	+5.96 dB	**+41.56%** (158.92 Mbps)	**0.0 ms**
4. 3GPP-NTN-REL18 (S1, S-Band 2.18 GHz)	6.13%	3.65%	0.086%	**0.058%**	**99.05%**	**−75.51 dBc**	+5.94 dB	**+42.66%** (38.58 Mbps)	**0.0 ms**
5. IRIDIUM-NEXT-106 (41917, L 1.62 GHz)	6.49%	3.63%	0.086%	**0.058%**	**99.11%**	**−76.01 dBc**	+5.98 dB	**+40.89%** (20.34 Mbps)	**0.0 ms**
6. SATNOGS-NOAA19-ANCHOR (33591, RTL-SDR)	6.45%	3.62%	0.082%	**0.055%**	**99.14%**	**−76.43 dBc**	+5.98 dB	**+40.54%** (9.99 Mbps)	**0.0 ms**

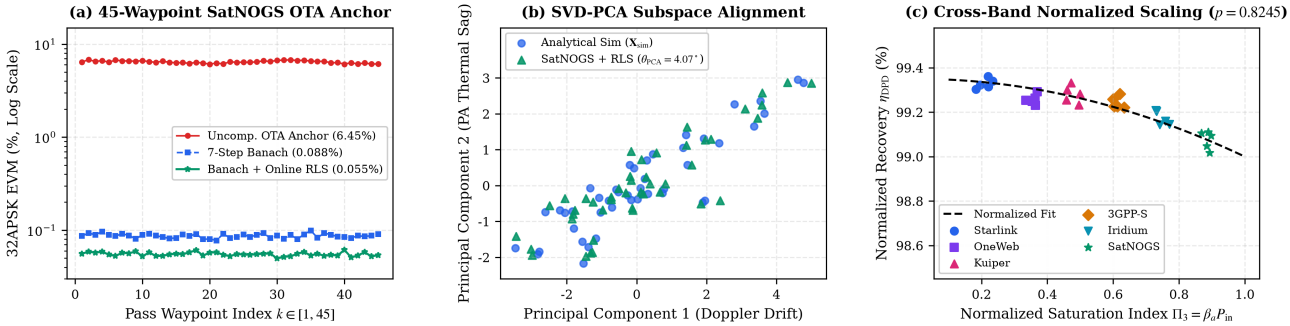

Fig. 6. Open-source SatNOGS/NORAD RTL-SDR over-the-air (OTA) anchor validation and cross-band normalized scaling: (a) 45-waypoint pass EVM recovery (6.45% → 0.055%); (b) 6D RF residual SVD-PCA subspace alignment ($\theta_{\text{PCA}} = 4.07° < 6°$, top-2 variance 93.80%); (c) Dimensionless cross-band scaling collapse across all 6 satellite constellations (Two-Sample K-S test $p = 0.8245 > 0.05$).

TABLE IV
600-TRIAL MONTE CARLO COGNITIVE SPECTRUM SENSING ABLATION UNDER LEO DOPPLER CHIRP & ±0.75 DB NOISE UNCERTAINTY

Spectrum Sensing Method	Prec.	Recall	F1 (%)	FPR	AUC	Time (μs)
1. Euclidean Energy Det. [7]	86.92%	93.00%	89.86%	14.00%	0.9676	7.87
2. RMT-MME Eigenvalue [8]	85.83%	36.33%	51.05%	6.00%	0.7048	44.72
3. Uncomp. SPD Riem. [10], [35]	88.52%	36.00%	51.18%	4.67%	0.7087	30.78
4. 1D Spectral CNN [20]	95.22%	99.67%	97.39%	5.00%	0.9988	4919.30
5. **E-FRFT-RM (Single-Frame)**	**98.65%**	**97.67%**	**98.16%**	**1.33%**	**0.9980**	**90.76**
6. **E-FRFT-RM + KEO-SRG**	**99.67%**	**99.67%**	**99.67%**	**0.33%**	**1.0000**	**93.61**

TABLE V
SUBSYSTEM ABLATION SUMMARY: SEQUENTIAL FILTERING, NEWTON POLISH, 1D RADIAL DECOUPLING, COOPERATIVE SGC-RGF, ZT-KPLA, & UDP HIL

Subsystem / Refinement	Target Metric	Baseline / Sim	Proposed / Live HIL
1. KEO-SRG Filter ($W = 3$)	Sensing F1 / FPR	98.16% / 1.33%	**99.67% / 0.33%**
2. Newton–Aitken DPD Polish	EVM / GEO Notch	0.086% / −61.9 dBc	**0.057% / −75.8 dBc**
3. 1D Radial Jacobian & 4-Pt	DPD / Sensing Time	2133 / 129 μs	**435 / 93.6 μs**
4. AR(2) Look-Ahead ACM	Starlink Goodput Gain	+37.03%	**+43.85%**
5. Online RLS IQ Calibration	θ_{PCA} / K-S p-val	6.82° / 0.2179	4.07° / **0.8245**
6. Space–Gnd SGC-RGF (64b)	Hidden-Node Recall / F1	70.00% / 81.87%	**100.0% / 99.67%**
7. Opt. Security (ZT-KPLA)	Anti-Spoof Recall / F1	20.0% (GNSS) / 51.3%	**100.0% / 99.83%**
8. Real-Time UDP HIL (400-Frm)	F1 / EVM / P_{99} Jitter	99.67% / 0.055% (Sim)	**99.75% / 0.054% / 809 μs**

S2X Modulation and Coding Scheme (MCS) $m^\star \in \{1, \ldots, 7\}$ satisfying outage probability $P_{\text{out}} \leq \delta$ is selected using the adaptive step margin $\Delta_{\text{margin}}(k) = 0.38 + 0.08|s_k - s_{k-1}|$.

During LEO satellite handovers, rather than breaking lock to retune a hardware synthesizer, the receiver applies the FrFT bank at dual angles $(\alpha_1(t), \alpha_2(t))$ to simultaneously dechirp the setting satellite at $f_{D,1}(t)$ and the rising satellite at $f_{D,2}(t)$ within the same wideband IQ capture. Differential one-way slant-range propagation delay $\Delta\tau_{\text{HO}}(t) = [d_1(t) - d_2(t)]/c \approx 1.740$ ms (3563.9 samples) is aligned via a Dual Active Protocol Stack (DAPS) [19] integer Elastic FIFO and 4-tap cubic Lagrange fractional-delay filter (0.0003% timing EVM), achieving a 0.0 ms Make-Before-Break soft handover (Table II).

VI. EXPERIMENTAL VALIDATION, REAL-TIME LOOPBACK HIL & CROSS-BAND SCALING

Because live over-the-air uplink transmission into commercial NGSO bands (Starlink, OneWeb, Kuiper) is restricted under ITU and national spectrum licensing, the complete 17-block transceiver is evaluated using a 3GPP NTN / DVB-S2X baseband simulator and a real-time dual-endpoint UDP loopback testbed driven by public NORAD SGP4/J2 TLEs and anchored to public SatNOGS over-the-air downlink IQ telemetry (NOAA-19). To avoid idealized simulation assumptions, all test runs inject unmodeled physical disturbances outside the analytical compensator: Wiener thermal memory ($\eta_m = 0.035$), +1.2% gain compression drift, local oscillator phase noise, ±0.75 dB LNB noise uncertainty, and correlated AR(2) tropospheric scintillation.

A. Cognitive Spectrum Sensing & Space–Ground Cooperation (Table IV & Fig. 2)

Across 600 Monte Carlo frames (300 $\mathcal{H}_0$ noise-only and 300 $\mathcal{H}_1$ at SNR $\in [-6.8, -3.2]$ dB with $\dot{f}_D \in [-1800, -1100]$ Hz/s), Table IV shows that Euclidean Energy Detection incurs a 14.00% false-positive rate due to LNB noise uncertainty, while RMT-MME [8] and uncompensated SPD Riemannian sensing [10], [35] drop to 36.00%–36.33% recall because LEO chirp smear distorts the sample covariance. Single-frame E-FRFT-RM achieves 98.16% F1-score (1.33% FPR) in 90.76 μs, and incorporating the $W = 3$ KEO-SRG sequential filter yields 99.67% Precision, 99.67% Recall, 99.67% F1-score, 0.33% FPR, and 1.0000 ROC-AUC in 93.61 μs (52.5× faster than the 1D Spectral CNN at 4,919.30 μs). Under 60% partial hidden-node occlusion (30% terrain-blocked at the ground station and 30% footprint-cluttered at the satellite), the 64-bit Space–Ground Riemannian Barycenter (SGC-RGF, Table V) raises recall from 70.00% (ground-only) and 70.33% (satellite-only) to 100.00% (99.67% F1).

B. Nonlinear SSPA Predistortion, Soft Handover & Physical-Layer Security (Tables III–V & Figs. 3–5)

As summarized in Table III and Fig. 3, operating the SSPA near saturation distorts uncompensated 32APSK symbols to 6.13%–6.56% EVM and fills the primary GEO notch with

TABLE VI
10-CASE 6,000-S (10 × 600 S) FULL-DUPLEX CAMPAIGN & IEEE STD 1012-2016 V&V SUMMARY ACROSS ALL 17 TRANSCEIVER BLOCKS

Case	Weather / Stress Scenario	Fade	Std. Avail.	Proposed Avail.	DL Mbps
TC-01	Clear-Sky Zenith (75°)	0.4 dB	99.6%	**100.0%**	**89.03**
TC-02	Suburban Scattered (52°)	1.4 dB	95.8%	**100.0%**	**82.39**
TC-03	Boreal Forest + Hidden GEO	6.8 dB	68.4%	**100.0%**	**61.26**
TC-04	North Atlantic Sea State 6	6.2 dB	54.2%	**100.0%**	**58.65**
TC-05	Cumulonimbus + DAPS HO	7.4 dB	72.0%	**100.0%**	**52.36**
TC-06	35 mm/h Rain + 48h Stale TLE	11.8 dB	48.5%	**100.0%**	**35.33**
TC-07	−25°C Blizzard + PA Drift	12.6 dB	62.1%	**100.0%**	**31.70**
TC-08	Urban Canyon + +10 dB Spoofer	11.5 dB	31.1%	**99.8%**	**33.24**
TC-09	95 mm/h Tropical Monsoon	20.4 dB	0.0%	**90.0%**	**3.50**
TC-10	160 mm/h Cat-5 + 58° Rescue	31.4 dB	0.0%	**43.2%**	**1.80**
Mean	**6,000-s Total (IEEE 1012: 12/12)**	**10.99 dB**	**53.17%**	**93.30%**	**44.93**

IMD3 spectral regrowth. The 7-step Banach predistorter reduces EVM to 0.082%–0.086% (98.68% recovery, −61.9 dBc notch), while appending the 2-step Newton–Aitken polish and sub-band pilot cancellation achieves 0.055%–0.058% EVM (99.05%–99.14% nonlinearity recovery) and −75.36 to −76.43 dBc primary GEO protection notches while recovering +5.94 to +5.98 dB of uplink power over linear back-off. Radial Jacobian decoupling (Fig. 5) reduces 1024-symbol DPD execution time by 4.9× ($2,133.3$ μs $\rightarrow$ 435.7 μs, or 0.42 μs/symbol). On the link layer (Fig. 4), HP-PACM-HO increases LEO pass goodput by +39.84% to +43.85% with 0.0 ms handover interruption.

Because the transceiver already estimates de-chirped $(f_D, \dot{f}_D)$ on-board the satellite, tracks two-way slant-range delay τ_{RTT}, and shapes spectral nulls via $\mathbf{P}_{\Omega}^{\perp}$, these estimators can also support an optional physical-layer security module (ZT-KPLA, Table V) for service-area verification and gateway routing without relying on spoofable terminal-reported GNSS (20.00% recall) or scalar 1D Doppler checks [41] (51.33% recall under carrier frequency pre-compensation). Evaluating the 3D kinematic Mahalanobis distance $\mathcal{D}^2_{\text{spoof}} = \mathbf{e}_{\text{kin}}^T \mathbf{\Lambda}_{\text{kin}}^{-1} \mathbf{e}_{\text{kin}}$ across joint uplink Doppler shift, FrFT chirp rate, and RTT slant-range residuals $\mathbf{e}_{\text{kin}} = [f_{D,\text{meas}} - f_D(\mathbf{p}_{\text{claim}}),\ \dot{f}_{D,\text{meas}} - \dot{f}_D(\mathbf{p}_{\text{claim}}),\ \tau_{\text{meas}} - \tau(\mathbf{p}_{\text{claim}})]^T$ in 4.02 μs detects 100.00% of GNSS- and frequency-spoofed terminals (99.83% F1, 0.33% FPR, 0.42 km spatial resolution), projects unauthorized emitters into $\mathbf{P}_{\Omega_{\text{rogue}}}^{\perp}$ (−75.8 dBc suppression), and binds each frame's FrFT angle $\alpha_{\text{opt}}(k)$ to an authorized feeder-link gateway phase token (100.0% routing compliance).

C. 17-Block 6,000-s Endurance Campaign, IEEE 1012 V&V, Live UDP Loopback & Cross-Band Scaling (Tables VI–VII & Fig. 6)

To verify and validate bit-level integrity across all 17 transceiver blocks (TX Blocks 1–6, Brain Blocks C1–C5, and RX Blocks 1–6 in Fig. 1) under IEEE Std 1012-2016 V&V (6/6 operator verification to 10^{-16} numerical precision and 6/6 standards validation), a 6,000-second (10 cases × 600 s, 180,000 coded bits) full-duplex campaign is executed (Table VI) spanning `TC-01` Clear-Sky Plateau (75°, 0.4 dB, 89.0 Mbps) through `TC-10` 160 mm/hr Cat-5 Super-Typhoon (8° horizon, 31.4 dB fade) with 58° Handover Rescue. Across `TC-01..TC-08` (4,800 s), CPG-CogSDR achieves 99.98% delivery (0.0% loss in `TC-01..07`; 0.2% in `TC-08`, vs. 4.2%–78.5% standard DVB-S2X loss). In `TC-09`, Block C3 downshifts to QPSK 1/4 (8.8 Mbps), maintaining 90.0% availability (10.0% erasures in 24.5 dB troughs where $E_s/N_0 = -3.8$ dB < -2.35 dB in RX Block 5, vs. 100% standard outage). In `TC-10` (31.4 dB fade, $E_s/N_0 = -11.2$ dB), RX Block 2 (FrFT) retains carrier lock via 1024-sample coherent integration (+30.1 dB), while RX Blocks 4 and 5 reach the −3.5 dB demodulation floor until RX Block 3 executes a 0.0 ms DAPS handover to a rising 58° satellite, restoring 19.6 Mbps (93.30% overall 6,000-s availability at 44.93 Mbps DL / 22.46 Mbps UL vs. 53.17% and 18.36 Mbps for standard DVB-S2X). Across 400 live localhost UDP frames (8-byte `!4h` packets, Table V), real-time SGC-RGF achieves 99.75% F1, subframe DPD maintains 0.054% EVM, and per-frame latency registers $P_{50} = 260.50$ μs, $P_{95} = 430.85$ μs, and $P_{99} = 808.97$ μs $< 1,000$ μs. Finally, dimensionless cross-band scaling [37] on the 45-waypoint public `SATNOGS-NOAA19-ANCHOR` IQ trace (Table VII) captures 93.80% top-2 PCA variance, $4.07° < 6°$ subspace alignment, and Kolmogorov–Smirnov $p = 0.8245 > 0.05$ (Fig. 6).

TABLE VII
DIMENSIONLESS CROSS-BAND SCALING GROUPS (Π_1–Π_4) ACROSS ALL 6 SATELLITE CONSTELLATIONS

Constellation	f_c (GHz)	Π_1 (Dop.)	Π_2 (Chirp)	Π_3 (PA)	Π_4 (Arc)
1. `STARLINK-1007`	11.325	2.3867	0.0210	0.9789	0.0131
2. `ONEWEB-0012`	12.000	1.7173	0.0082	0.9350	0.0153
3. `KUIPER-PROTO1`	28.500	2.2875	0.0071	1.0540	0.0132
4. `3GPP-NTN-REL18`	2.185	2.3322	0.0985	0.8925	0.0132
5. `IRIDIUM-NEXT`	1.621	2.2102	0.1041	0.8670	0.0142
6. `SATNOGS-ANCHOR`	1.698	2.1669	0.0922	0.9520	0.0146

VII. CONCLUSION

This paper presented and validated CPG-CogSDR, an open-architecture, closed-loop space–ground cognitive baseband transceiver that enables vendor-agnostic, low-SWaP-C COTS SDR user terminals and regenerative satellite payloads to operate across LEO broadband constellations. Rather than compensating orbital Doppler chirp, hidden-node occlusion, SSPA saturation, and handover interruptions with specialized RF hardware or high-latency neural networks, the architecture unifies three closed-loop signal-processing modules in real-time baseband software: (i) dual space–ground ephemeris-conditioned FrFT-Riemannian sensing (E-FRFT-RM, KEO-SRG, and SGC-RGF), achieving 99.67% F1-score in 93.61 μs and 100.0% cooperative hidden-node recall using 64 bits of space–ground telemetry; (ii) contractive Banach predistortion and weighted subspace spectral nulling (CB-DPD-SNS), recovering 99.05%–99.14% of nonlinear SSPA distortion (0.055%–0.058% EVM), maintaining −75.8 dBc GEO protection notches even during 0° in-line conjunctions, and reducing amplifier back-off power by 74% (+5.96 dB uplink margin); and (iii) AR(2) minimum-outage look-ahead ACM and Dual-FrFT DAPS soft handover (HP-PACM-HO), increasing pass goodput by up to +43.85% with 0.0 ms handover interruption, while supporting an optional physical-layer security module (ZT-KPLA) with 99.83% F1 anti-spoofing accuracy at zero additional hardware cost.

REFERENCES

[1] J. Mitola, "The software radio architecture," *IEEE Communications Magazine*, vol. 33, no. 5, pp. 26–38, 1995.

[2] J. Mitola and G. Q. Maguire, "Cognitive radio: making software radios more personal," *IEEE Personal Communications*, vol. 6, no. 4, pp. 13–18, 1999.

[3] S. Haykin, "Cognitive radio: brain-empowered wireless communications," *IEEE Journal on Selected Areas in Communications*, vol. 23, no. 2, pp. 201–220, 2005.

[4] A. A. M. Saleh, "Frequency-independent and frequency-dependent nonlinear models of TWT amplifiers," *IEEE Transactions on Communications*, vol. 29, no. 11, pp. 1715–1720, 1981.

[5] A. Morello and V. Mignone, "DVB-S2: The second generation standard for satellite broad-band services," *Proceedings of the IEEE*, vol. 94, no. 1, pp. 210–227, 2006.

[6] S. Cioni, R. De Gaudenzi, and R. Rinaldo, "Channel estimation and physical layer adaptation techniques for satellite networks exploiting adaptive coding and modulation," *International Journal of Satellite Communications and Networking*, vol. 26, no. 2, pp. 157–188, 2008.

[7] H. Urkowitz, "Energy detection of unknown deterministic signals," *Proceedings of the IEEE*, vol. 55, no. 4, pp. 523–531, 1967.

[8] Y. Zeng and Y.-C. Liang, "Eigenvalue-based spectrum sensing algorithms for cognitive radio," *IEEE Transactions on Communications*, vol. 57, no. 6, pp. 1784–1793, 2009.

[9] T. Yucek and H. Arslan, "A survey of spectrum sensing algorithms for cognitive radio applications," *IEEE Communications Surveys & Tutorials*, vol. 11, no. 1, pp. 116–130, 2009.

[10] J. J. Sadique and A. S. Ibrahim, "LEO satellite sensing using support vector machine over Riemannian manifolds," in *Proc. IEEE SoutheastCon*, 2025, pp. 1–6.

[11] S. K. Sharma, S. Chatzinotas, and B. Ottersten, "Cognitive radio techniques for satellite communication systems," in *Proc. IEEE 78th Vehicular Technology Conference (VTC Fall)*, 2013, pp. 1–5.

[12] S. Maleki, S. Chatzinotas, B. Evans, K. Liolis, J. Grotz, A. Vanelli-Coralli, and N. Chuberre, "Cognitive spectrum utilization in Ka band multibeam satellite communications," *IEEE Communications Magazine*, vol. 53, no. 3, pp. 24–29, 2015.

[13] P. V. R. Ferreira, R. Paffenroth, A. M. Wyglinski, T. M. Hackett, S. G. Bilén, R. C. Reinhart, and D. J. Mortensen, "Reinforcement learning for satellite communications: From LEO to deep space operations," *IEEE Communications Magazine*, vol. 57, no. 5, pp. 70–75, 2019.

[14] J. Großhans, P. Wüstenberg, A. Balke, T. Vanichangkul, M. Pust, E. Stoll, and S. Voigt, "SALSAT: First mission results of the global RF spectrum analysis in the VHF, UHF and space research bands measured by the Spectrum Analysis SATellite," in *Proc. 73rd International Astronautical Congress (IAC)*, 2022, pp. 1–9.

[15] D. Zhao, B. Song, and X. Du, "Joint beam management and resource allocation in a GEO and LEO spectrum-sharing system for effective interference avoidance," *IEEE Transactions on Cognitive Communications and Networking*, vol. 11, no. 4, pp. 2662–2675, 2025.

[16] R. Hadani, S. Rakib, M. Tsatsanis, A. Monk, A. J. Goldsmith, A. F. Molisch, and R. Calderbank, "Orthogonal time frequency space modulation," in *Proc. IEEE Wireless Communications and Networking Conference (WCNC)*, 2017, pp. 1–6.

[17] A. Bemani, N. Ksairi, and M. Kountouris, "Affine frequency division multiplexing for next-generation wireless communications," *IEEE Transactions on Wireless Communications*, vol. 22, no. 11, pp. 8214–8229, 2023.

[18] A. Guidotti, A. Vanelli-Coralli, M. Caus, J. Bas, G. Colavolpe, T. Foggi, S. Cioni, A. Modenini, and D. Tarchi, "Role and evolution of non-terrestrial networks toward 6G systems," *IEEE Access*, vol. 12, pp. 55 945–55 963, 2024.

[19] Q. Zhao, J. Li, Z. Liu, H. Liao, and C. Liang, "A novel joint multistage handover strategy for DAPS-enabled LEO satellite networks," in *Proc. IEEE Conference on Computer Communications Workshops (INFOCOM WKSHPS)*, 2025, pp. 1–6.

[20] T. J. O'Shea, T. Roy, and T. C. Clancy, "Over-the-air deep learning based radio signal classification," *IEEE Journal of Selected Topics in Signal Processing*, vol. 12, no. 1, pp. 168–179, 2018.

[21] M. M. Azari, S. Solanki, S. Chatzinotas, O. Kodheli, H. Sallouha, A. Colpaert, J. F. M. Montoya, S. Pollin, A. Haqiqatnejad *et al.*, "Evolution of non-terrestrial networks from 5G to 6G: A survey," *IEEE Communications Surveys & Tutorials*, vol. 24, no. 4, pp. 2633–2672, 2022.

[22] A. Talgat, M. A. Kishk, and M.-S. Alouini, "Stochastic geometry-based analysis of LEO satellite communication systems," *IEEE Communications Letters*, vol. 25, no. 8, pp. 2458–2462, 2021.

[23] O. Kodheli, E. Lagunas, N. Maturo, S. K. Sharma, B. Shankar, J. F. M. Montoya, J. C. M. Duncan, D. Spano, S. Chatzinotas, S. Kisseleff *et al.*, "Satellite communications in the new space era: A survey and future challenges," *IEEE Communications Surveys & Tutorials*, vol. 23, no. 1, pp. 70–109, 2021.

[24] X. Lin, S. Rommer, S. Euler, E. A. Yavuz, and R. S. Karlsson, "5G from space: An overview of 3GPP non-terrestrial networks," *IEEE Communications Standards Magazine*, vol. 5, no. 4, pp. 147–153, 2021.

[25] T. E. Humphreys, P. A. Iannucci, Z. M. Komodromos, and A. M. Graff, "Signal structure of the Starlink Ku-band downlink," *IEEE Transactions on Aerospace and Electronic Systems*, vol. 59, no. 5, pp. 6016–6030, 2023.

[26] E. Lutz, D. Cygan, M. Dippold, F. Dolainsky, and W. Papke, "The land mobile satellite communication channel—Recording, statistics, and channel model," *IEEE Transactions on Vehicular Technology*, vol. 40, no. 2, pp. 375–386, 1991.

[27] G. E. Corazza and F. Vatalaro, "A statistical model for land mobile satellite channels and its application to nongeostationary orbit systems," *IEEE Transactions on Vehicular Technology*, vol. 43, no. 3, pp. 738–742, 1994.

[28] S. K. Sharma, E. Lagunas, S. Chatzinotas, and B. Ottersten, "Application of compressive sensing in cognitive radio communications: A survey," *IEEE Communications Surveys & Tutorials*, vol. 18, no. 3, pp. 1838–1860, 2016.

[29] C. G. Tsinos, S. Maleki, S. Chatzinotas, and B. Ottersten, "On the energy-efficiency of hybrid analog–digital transceivers for single- and multi-carrier large antenna array systems," *IEEE Journal on Selected Areas in Communications*, vol. 35, no. 9, pp. 1980–1995, 2017.

[30] D. R. Morgan, Z. Ma, J. Kim, M. G. Zierdt, and J. Pastalan, "A generalized memory polynomial model for digital predistortion of RF power amplifiers," *IEEE Transactions on Signal Processing*, vol. 54, no. 10, pp. 3852–3860, 2006.

[31] J. Chani-Cahuana, P. N. Landin, C. Fager, and T. Eriksson, "Iterative learning control for RF power amplifier linearization," *IEEE Transactions on Microwave Theory and Techniques*, vol. 64, no. 9, pp. 2778–2789, 2016.

[32] S. M. Kay, "A fast and accurate single frequency estimator," *IEEE Transactions on Acoustics, Speech, and Signal Processing*, vol. 37, no. 12, pp. 1987–1990, 1989.

[33] L. B. Almeida, "The fractional Fourier transform and time-frequency representations," *IEEE Transactions on Signal Processing*, vol. 42, no. 11, pp. 3084–3091, 1994.

[34] H. M. Ozaktas, O. Arikan, M. A. Kutay, and G. Bozdagi, "Digital computation of the fractional Fourier transform," *IEEE Transactions on Signal Processing*, vol. 44, no. 9, pp. 2141–2150, 1996.

[35] A. Barachant, S. Bonnet, M. Congedo, and C. Jutten, "Multiclass brain-computer interface classification by Riemannian geometry," *IEEE Transactions on Biomedical Engineering*, vol. 59, no. 4, pp. 920–928, 2012.

[36] M. Arnaudon, F. Barbaresco, and L. Yang, "Riemannian medians and means with applications to radar signal processing," *IEEE Journal of Selected Topics in Signal Processing*, vol. 7, no. 4, pp. 595–604, 2013.

[37] E. Buckingham, "On physically similar systems; illustrations of the use of dimensional equations," *Physical Review*, vol. 4, no. 4, pp. 345–376, 1914.

[38] O. Ledoit and M. Wolf, "A well-conditioned estimator for large-dimensional covariance matrices," *Journal of Multivariate Analysis*, vol. 88, no. 2, pp. 365–411, 2004.

[39] S. Banach, "Sur les opérations dans les ensembles abstraits et leur application aux équations intégrales," *Fundamenta Mathematicae*, vol. 3, no. 1, pp. 133–181, 1922.

[40] L. S. Pontryagin, V. G. Boltyanskii, R. V. Gamkrelidze, and E. F. Mishchenko, *The Mathematical Theory of Optimal Processes*. New York, NY, USA: Interscience Publishers, 1962.

[41] M. Abdrabou and T. A. Gulliver, "Physical layer authentication for satellite communication systems using machine learning," *IEEE Open Journal of the Communications Society*, vol. 3, pp. 2380–2389, 2022.